Light Curve Analysis of Deep Space Objects in Complex Rotation States

Michael D. Abercrombie[1], **Brandoch Calef**[1], **and Shadi Naderi**[2]
[1]*The Boeing Company, 550 Lipoa Pkwy, Kihei, HI 96753*
[2]*Air Force Research Laboratory, 550 Lipoa Pkwy, Kihei, HI 96753*

ABSTRACT

Characterization of non-resolvable Earth-orbiting space objects represents an essential capability in the domain of Space Situational Awareness (SSA). Techniques that exploit photometric light curves of reflected sunlight can be used to passively provide a wide range of useful information about this ever-growing population, including the rotation state of the object, which can be helpful for assessing the intent of a non-cooperative target, improving long-term orbit projections, on-orbit debris mitigation efforts, or planning satellite servicing missions. Part of this effort includes the ability to objectively discriminate between a stable, single axis spin state and complex rotation about multiple axes in cases where periodic behavior is detected.

Light curve models of multiaxis rotation are presented for several GOES 8 observations made from meter-class telescopes at the Maui Space Surveillance Center located at the summit of Haleakalā. GOES 8 is a retired communications satellite near geosynchronous Earth orbit (GEO) whose rapidly evolving complex rotation state has been well established, making it an excellent candidate for studies of multiaxis rotation. Clear evidence of complex rotation was obtained, and estimates of the spin and precession periods best describing these observations are provided.

1. BACKGROUND

In the domain of Space Situational Awareness (SSA), knowledge about the rotation state of a space object can help determine whether or not an object is operating in an active state, potentially useful in assessing the intent of a non-cooperative satellite. For instance, because spin-stabilized satellites typically maintain a constant spin rate, a long term increase in period may indicate that a satellite is inactive. Complex, tumbling motion is another potential indication that a satellite is not in an active state. Furthermore, studies of defunct satellite spin state evolution can improve long-term orbit projections, on-orbit debris mitigation efforts, and potential satellite servicing missions [1, 2, 3]. Characterization of a satellite's spin state has also proven useful in anomaly resolution [4].

The results shown here were part of larger software validation effort which involved analysis of photometric observations of non-resolvable objects in a range of orbital regimes and spacecraft attitudes. With regards to complex rotation, the goals of this campaign were to successfully discern objects in complex spin states from those undergoing stable, single axis rotation using only the object's light curve and other data contained in a standard EOSSA file [5], and to identify the characteristic spin and precession periods of these tumbling objects. The algorithms that have been developed do not rely on any prior spacecraft model information so that they may be as effective describing an unknown target as one that is known.

2. THEORY

The theory and algorithms used to characterize the rotation state of a time-resolved photometric observation are now presented. After an initial determination of the presence of a periodic signature, the most likely single-frequency period is used to obtain a model of the measured light curve. In cases where this model is a poor fit to the data, a search for a multiaxis spin state solution, indicating a complex tumbling state, is performed. A comparison to previously processed data is used to indicate a potential change in rotation state. And finally, in cases where a single-frequency solution is preferred, indicating the presence of a stable spin state, small variations in this best-fit period caused by changes in the observational geometry can be exploited to obtain the true, *sidereal* period of rotation, as well as the spin axis orientation. All algorithms described here have been developed to handle scenarios where no shape or reflectivity information about the observed object is provided, lending themselves well to characterization of unknown objects.

Approved for public release; distribution is unlimited. Public Affairs release approval #AFRL-2021-3059.

2.1 Determining periodicity

The first step in the periodicity analysis algorithm is to search for statistically-significant periodic features in the light curve, an indication that the observed object is undergoing rotational motion. This is accomplished using a Lomb-Scargle periodogram, which produces a frequency spectrum similar to that generated by fast-Fourier transforms, but is better-suited to handle noisy and irregularly sampled data. The presence of peaks in the periodogram power spectrum above a power level describing a specified probability threshold initiates a process for creating a periodic model of the measured light curve. Harmonic ambiguities, which often arise from light curves with multiple brightness maxima per cycle, are addressed by considering harmonics of dominant peaks in the periodogram power spectrum as candidate frequencies.

Prominent frequencies from the Lomb-Scargle periodogram are used to generate candidate light curve models comprised of a low-order polynomial fit, to remove non-periodic drift in the light curve, and a Fourier series which describes periodic features. Such models have the form

$$f(t) = \sum_{m=0}^{N_P} a_m (t-t_0)^m + \sum_{n=1}^{N_F} \left[b_n \cos\left[n\omega (t-t_0)\right] + c_n \sin\left[n\omega (t-t_0)\right]\right] \tag{1}$$

where the coefficients a_m, b_n, and c_n are chosen during a least-squares fitting process for each of the most significant candidates frequencies from the power spectrum. The number of polynomial and Fourier terms, n_p and n_f respectively, are chosen by maximum Bayesian evidence with preference for simpler models in the absence of compelling evidence for additional terms. The reference time t_0 is arbitrary but is usually chosen as the time of the first measurement. As usual, the period of the model T is related to the angular frequency by $T = 2\pi/\omega$. Candidates models are refined by sampling the space near each candidate frequency and then ranked using the Bayesian regression algorithm [6]. The relative probability between models is determined using a combination of this evidence ranking and a goodness of fit ranking based on Root Mean Square and Median Absolute deviations.

At this point in the analysis the model describing the best single-frequency solution to the light curve is compared to a model containing only low-order polynomial terms. Along with the existence of statistically-significant peaks in the light curve power spectrum, a preference for the model including periodic terms leads to the declaration of periodicity in the observed light curve. The period of this best fit model is chosen as the most probable period in the case of an object in a stable spin state and additional analysis may then be performed to further characterize the rotation state of the object.

2.2 Synodic period variations

Assuming a stable spin state, changes in the sun-object-observer geometry may lead to variations in the measured synodic period of the object which can be exploited to provide information about sidereal period and the spin axis orientation of the object. This phenomenon most often applies to objects in low-Earth orbit where rapidly changing geometries are present. To detect variations in the synodic period, model solutions of the form given in Equation 1 are fit to subsets of the full light curve. Starting from the previously determined best fit period, ω is refined via a maximum evidence search independently for each subset until the entire length of the light curve has been covered. If found, changes in the synodic period over the length of the light curve are used for additional analysis of the object's spin state.

2.3 Multiaxis spin state analysis

The next step in the periodicity analysis processing sequence includes an assessment of the likelihood that the light curve represents a complex spin state requiring a multi-frequency model. The multiaxis spin state analysis considers the RMSD and MAD of the best single frequency model to grade the quality of the fit; if the existing model provides a sufficiently good fit to the data, a stable single-axis spin state is declared. If the fit of the single frequency model is not an adequate fit to the light curve but synodic period variations were detected, a stable single-axis spin state is declared with perceived frequency variation resulting from changing sun-object-observer geometry. If the sliding frequency model does adequately describe the observed light curve, or synodic period variations were not detected, a multi-frequency model is considered.

Following Pravec et al. [7], the light curve of tumbling object can be described by two frequencies representing the spin and average precession angular frequencies, ω_Ψ and $\omega_{\bar{\phi}}$, respectively

Approved for public release; distribution is unlimited. Public Affairs release approval #AFRL-2021-3059.

$$f(t) = \sum_{m=0}^{n_p} a_m (t-t_0)^m + \sum_{j=1}^{n_f} \left[b_{j0} \cos\left[j\omega_\Psi (t-t_0) \right] + c_{j0} \sin\left[j\omega_\Psi (t-t_0) \right] \right] + \sum_{k=1}^{n_f} \sum_{j=-n_f}^{n_f} \left[b_{jk} \cos\left[\left(j\omega_\Psi + k\omega_{\tilde{\phi}} \right) (t-t_0) \right] + c_{jk} \sin\left[\left(j\omega_\Psi + k\omega_{\tilde{\phi}} \right) (t-t_0) \right] \right] \quad (2)$$

The same least-squares approach is used to locate the optimal choices of ω_Ψ and $\omega_{\tilde{\phi}}$ from peaks chosen from the light curve power spectrum, as well as coefficients a_m, b_{jk}, and c_{jk}, and the number of terms, given by $n_p + \left(2n_f + 1\right)^2$. Upon settling on the best two-frequency model for the provided light curve, this model is compared to the best single frequency model using a combination of Bayesian evidence and RMSD and MAD quality of fit probabilities to determine the relative probability of the spin state of the object. The quality of the fit of the preferred model is then used to report a confidence in the chosen model.

2.4 Relative probability

The relative probability between a list of candidate light curve models is calculated using a combination of the probability from the Bayesian evidence for each model, and the probability from the quality of the fit as determined by the Root Mean Square and Median Average deviations

$$\sigma_{RMS} = \left[\frac{1}{n} \sum_{i=1}^{n} \left(y - y' \right)^2 \right]^{1/2} \quad (3)$$

and

$$\sigma_{MA} = k \cdot \text{ median} \left(|\Delta y - \widetilde{\Delta y}| \right) \quad (4)$$

where $k = 1/\Phi^{-1}(3/4) \approx 1.4826$. Δy gives the model residuals, the difference between measured magnitudes y and light curve model values y', and $\widetilde{\Delta y}$ gives the median value of Δy.

Chi-squared estimates are given by $\chi^2_{RMS} = \sigma^2_{RMS}$ and $\chi^2_{MA} = \sigma^2_{MA}$, and relative likelihoods for $i = 1, 2, ..., n_c$ candidate models from χ^2 values are given by

$$f^{(i)}_{RMS,rel} = \frac{1}{2} e^{\left(\chi^2_{RMS,i} - \chi^2_{RMS,best} \right)/2} \quad \text{and} \quad f^{(i)}_{MA,rel} = \frac{1}{2} e^{\left(\chi^2_{MA,i} - \chi^2_{MA,best} \right)/2} \quad (5)$$

where $\chi^2_{RMS,best}$ and $\chi^2_{MA,best}$ represent an explicitly chosen *best* candidate solution, or the solution with the maximum evidence E. Absolute χ^2 probabilities for each model based on grading the signal-to-noise fit are given by

$$f^{(i)}_{RMS,abs} = 1 - F\left(\chi^2_{RMS} | \nu \right) \quad \text{and} \quad f^{(i)}_{MA,abs} = 1 - F\left(\chi^2_{MA} | \nu \right) \quad (6)$$

where the cumulative distribution function of the χ^2-distribution $F(x|\nu)$ gives the probability that a single observation with ν degrees of freedom falls within the interval $[0, x]$

$$F(x|\nu) = \int_0^x \frac{t^{(\nu-2)/2} e^{-t/2}}{2^{\nu/2} \Gamma(\nu/2)} dt. \quad (7)$$

The probability derived from the quality of fit of each model $\mathbf{P}^{(i)}_f$ is the maximum value from the four probabilities described in Equations 5 and 6, clipped at an upper limit of 1.

Approved for public release; distribution is unlimited. Public Affairs release approval #AFRL-2021-3059.

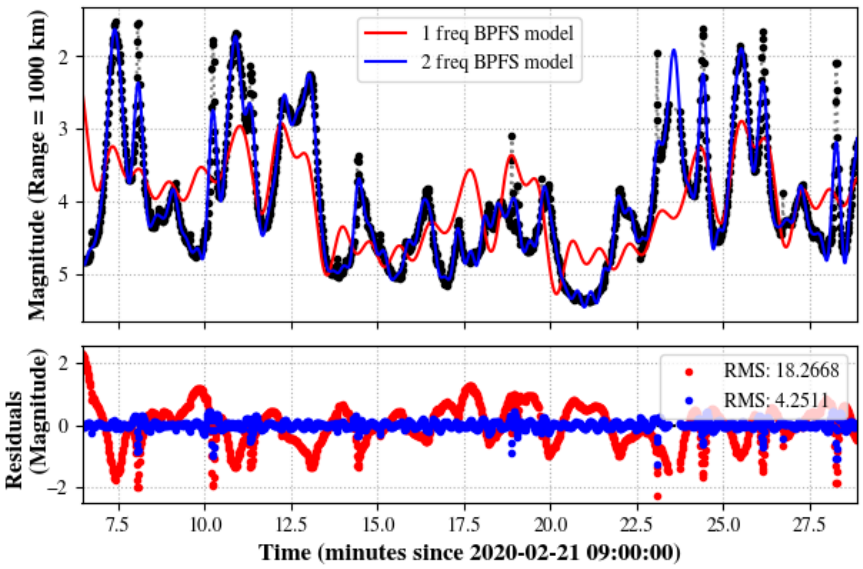

Fig. 1: A comparison between the best single-frequency model (in red) and two-frequency model (in blue) for the 21 Feb 2020 GOES 8 collection. The model residuals are shown below, clearly illustrating the improvement obtained by using the two-frequency model. Based on the light curve models shown here, a complex spin state is declared in favor of a stable spin state with a $> 99.99\%$ probability.

The evidence-based probability is given by

$$\mathbf{P}_E^{(i)} = e^{(E_i - E_{max})} \tag{8}$$

The relative probability of each model in a set of candidate models is given by

$$\mathbf{P}'^{(i)} = \begin{cases} \left(\mathbf{P}_f^{(i)} + \mathbf{P}_E^{(i)}\right)/2 & \text{if } \mathbf{P}_E^{(i)} < \mathbf{P}_f^{(i)} \\ \mathbf{P}_f^{(i)} & \text{if } \mathbf{P}_E^{(i)} \geq \mathbf{P}_f^{(i)}. \end{cases} \tag{9}$$

A prior probability p_p which penalizes solutions with periods longer than the maximum evidence candidate is applied to each $\mathbf{P}'^{(i)}$. This prior is given by $p_p = p^*/p^{(i)}$ where p^* gives the minimum of all model periods which have at least the same confidence as the best model, and $p^{(i)}$ represents the periods of each model solution. The relative probability from Equation 9 is then updated by

$$\mathbf{P}^{(i)} = p_p \mathbf{P}'^{(i)}. \tag{10}$$

At this point values of $\mathbf{P}^{(i)}$ are clipped at $\mathbf{P}_{best}^{(i)}$ and normalized to ensure that $\sum_{i=1}^{n_c} \mathbf{P}^{(i)} = 1$.

3. OBSERVATIONS AND MODELS

GOES 8 is a retired weather satellite in a geosynchronous earth orbit (GEO) whose complex rotation state has been well-established [1, 2, 3]. As shown over a period of several years, the GOES 8 spin state evolves rapidly. It is hypothesized that this evolution results from the Yarkovsky-O'Keefe-Radzievskii-Paddock (YORP) effect, which is known to affect the spin states of asteroids, and involves external torques generated by the absorption, reflection, and thermal re-emission of solar radiation [8, 9]. GOES 8 was chosen as a target with which to validate the performance of the multiaxis spin state analysis algorithms.

Approved for public release; distribution is unlimited. Public Affairs release approval #AFRL-2021-3059.

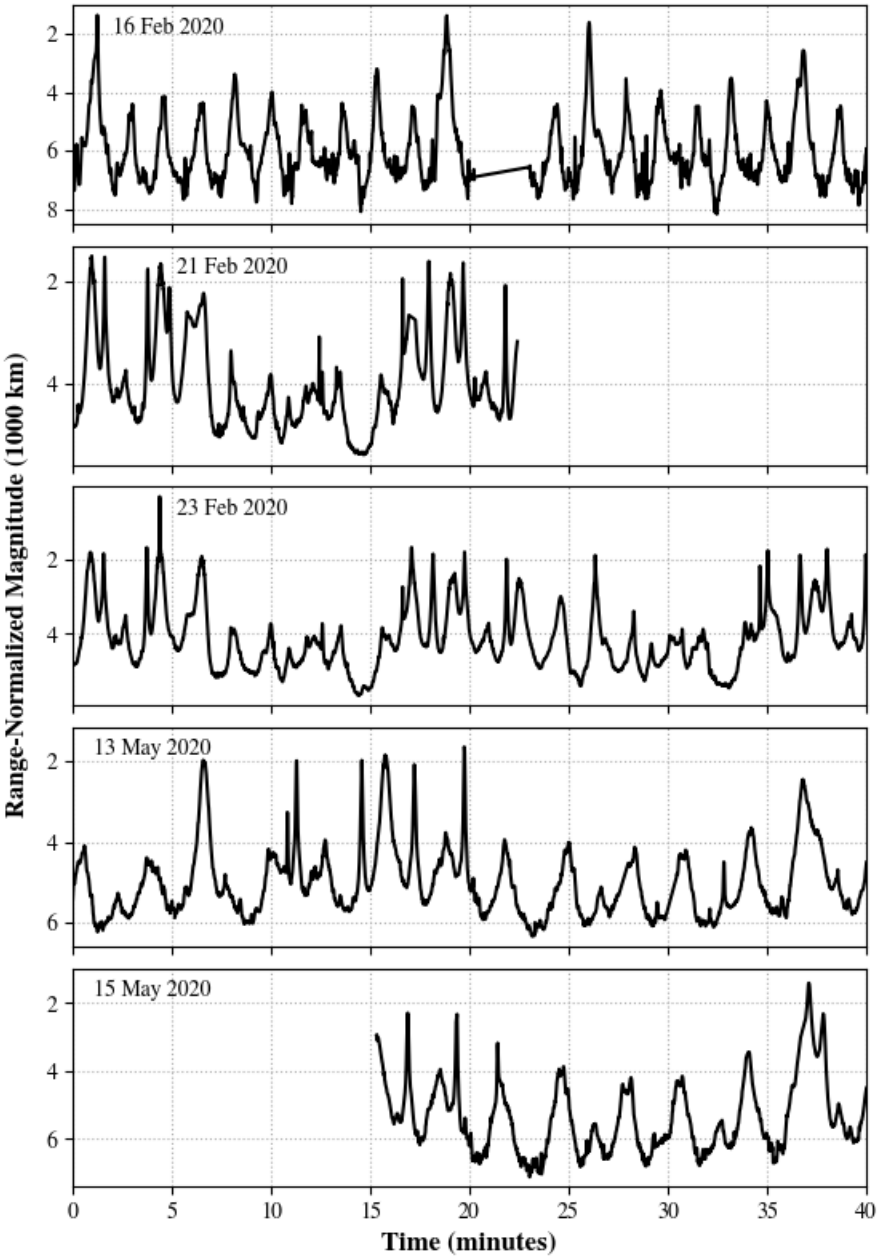

Fig. 2: Portions of each GOES 8 light curve collected during this effort. Light curves have been shifted in phase to maximize cross correlation between the preceding observation. The date of each observation is given in the upper left of each plot.

Observations of the GOES 8 satellite were collected at the Air Force Maui Optical and Supercomputing Observatory (AMOS) using the US Air Force's 1.6-meter telescope located on the summit of Haleakalā on Maui. Photometric measurements were collected on five nights between 16 February 2020 and 15 May 2020 on the wide field of view (WFOV) JAWS sensor; a 1110S series CCD camera produced by Spectral Instruments Inc. which uses a Teledyne e2v CCD44-82 back illuminated, non-inverted mode operation CCD sensor with 2048×2048 pixels which can be binned in 1×1 or 2×2 configurations. The sensor is sensitive from 400 to 1000 nm with an average quantum efficiency of greater than 70% over that range. Calibration of all GOES 8 datasets was performed by software using a sophisti-

Approved for public release; distribution is unlimited. Public Affairs release approval #AFRL-2021-3059.

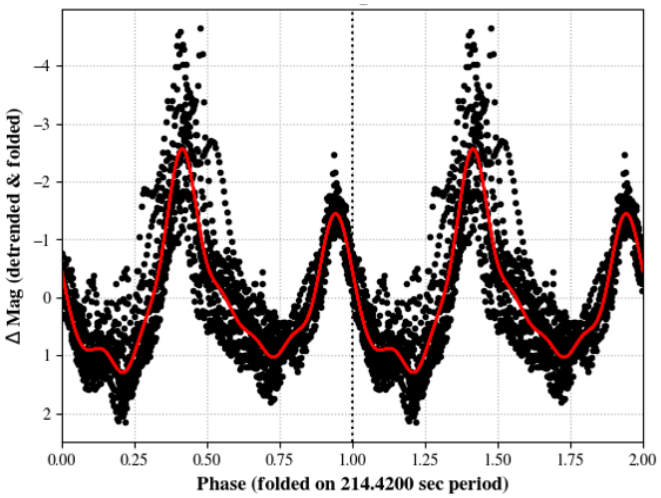

Fig. 3: GOES 8 light curve collected on 16 Feb 2020 and folded on a 214.420 second period. Two phases of this suspected precession period are shown.

cated star matching algorithm and differential photometry to remove atmospheric attenuation from the photometric measurements.

Portions of the range-normalized light curves from each of the five nights of GOES 8 collections are shown in Figure 2. The light curves have been aligned to maximize cross-correlation between subsequent observations to illustrate similarities, particularly between collections obtained within a couple days of each other (see February 21 and 23 and May 13 and 15). Spin state parameters $T_{\bar{\phi}}$ and T_{Ψ} should be relatively consistent where light curve similarities are apparent.

3.1 Determining $T_{\bar{\phi}}$

The 52.7 minute collection obtained on February 16 (a portion of which is shown in the top plot of Figure 2) appears to resemble a uniform spin state better than any of the other four collections, thus offering perhaps the best opportunity to determine the period $T_{\bar{\phi}}$ associated with the evolving complex spin state of GOES 8. The dominant peak in the raw periodogram spectrum f_* corresponds to a period of 107.217 seconds. By also considering the first 4 harmonics of this spectrum, the top three maximum evidence models have periods of $8f_*^{-1}$, $4f_*^{-1}$, and $2f_*^{-1}$, respectively. Based on the known geometry of the GOES 8 satellite bus, as well as the findings of Benson et al., the $4f_*^{-1}$ or $2f_*^{-1}$ model is most likely accurate, with the expectation that the complex rotation state of the satellite will prevent clean folding of the light curve on the true average precession period and lead to a preference for a longer period. When the quality of fit metrics, RMS and MA deviation, are considered, twice the peak frequency, or a period of 214.420 seconds, is preferred. The folded light curve shown in Figure 3 illustrates the feasibility of this model.

The next GOES 8 collection was obtained 5 days later, on February 21. This 23.9 minute collection has a far more chaotic signature, with no real semblance of uniform rotation. The dominant peak in the raw power spectrum corresponds to a period of 108.671 seconds, with $T_{\bar{\phi}} = 217.393$ seconds found as the most likely solution that is an integer multiple of this peak. This precession period represents a 2.973 second increase over a five day span.

Two days later a 71.1 minute collection was obtained with additional low frequency patterns apparent in the light curve. The upper left plot in Figure 4 shows the February 23 collection folded on the maximum evidence, 1094.900 second period. Since previous collections rule out a stable spinner with a $\sim$10 peak periodic signature, this period most likely corresponds to the quasi-period, defined as

$$\overline{T} \approx mT_{\bar{\phi}} \approx nT_{\Psi} \tag{11}$$

where m and n represent integers which describe the length of time required for the satellite to return to nearly the same inertial attitude [2]. The model with the next highest Bayesian evidence has a period of $2f_*^{-1} = 219.440$ seconds, corresponding to $m = 5$ in Equation 11 and a 2.447 second increase over the suspected $T_{\bar{\phi}}$ from the previous observation.

Approved for public release; distribution is unlimited. Public Affairs release approval #AFRL-2021-3059.

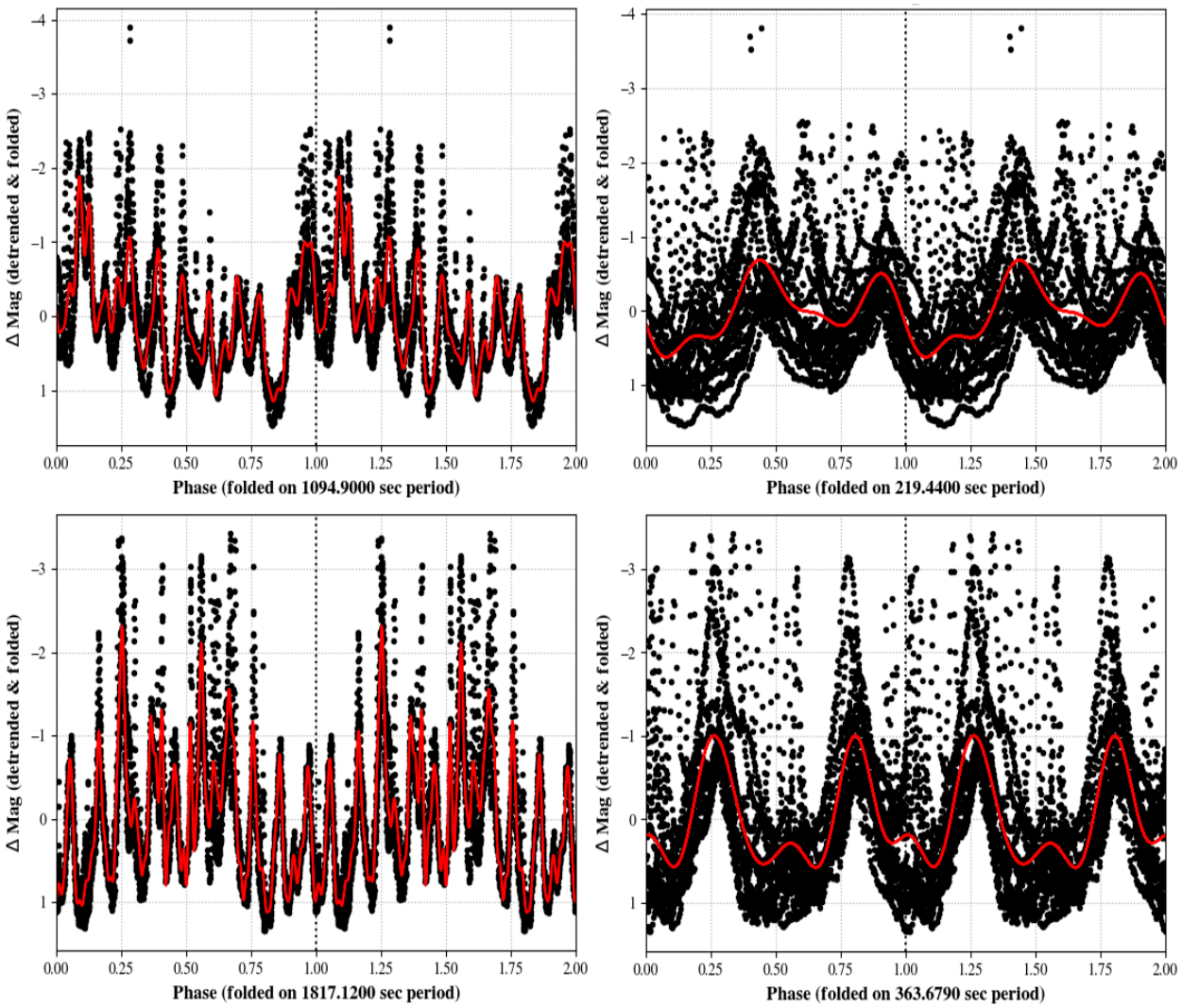

Fig. 4: Top: GOES 8 light curve collected on 23 Feb 2020 and folded on a 1094.900 second suspected quasi-period (left) and 219.440 second precession period (right). Bottom: GOES 8 light curve collected on 13 May 2020 folded on the suspected 1817.120 second quasi-period (left) and 363.679 second precession period (right).

In theory, a full rotation state model can be determined by comparing the quality of models with $T_\Psi \approx \overline{T}/n$.

The next observation of GOES 8 was made on May 13. This light curve spans 107.6 minutes, and like all other GOES 8 light curves collected is clearly identified as a complex rotation state. Like the February 23 collection, the maximum evidence single frequency model appears to represent the quasi-period, with at least 10 significant peaks occurring in the light curve signature when folded on this 1817.120 second period. The $2f_*^{-1}$ period here is equal to 363.679 seconds, again with $m = 5$. This precession period represents a 144.239 second increase over the previous 80 days. This corresponds to an average increase of 1.8 seconds/day, indicating that the precession period is increasing at an accelerating rate. The bottom plots in Figure 4 show the May 13 light curve folded on the suspected quasi-period and precession period.

The final GOES 8 collection was obtained two days later, on May 15. Spanning 60.3 minutes, this light curve aligns nicely with the May 13 collection as shown in Figure 2. The $2f_*^{-1}$ period of 369.045 seconds is 5.366 seconds longer than the previous $T_{\bar{\phi}}$ estimate.

Approved for public release; distribution is unlimited. Public Affairs release approval #AFRL-2021-3059.

Table 1: GOES 8 precession and spin periods determined via investigation of maximum evidence single frequency models and periodogram power spectrum results. Here * indicates a period that has been estimated based on previously measured results.

Date	Length (min)	$T_{\bar{\phi}}$ (s)	T_{Ψ} (s)
2020-02-16	52.7	214.569 ± 7.274	1054.97 ± 175.828
2020-02-21	23.9	217.393 ± 0.826	1087^{*}
2020-02-23	71.1	218.902 ± 5.613	1067.150 ± 133.393
2020-05-13	107.6	363.679 ± 0.199	1818^{*}
2020-05-15	60.3	369.045 ± 0.365	1845^{*}

3.1.1 Determining T_{ψ}

The suspected quasi-periods shown in Figure 4 for the Feb 23 and May 13 observations offered a starting point for narrowing down candidate spin periods for the presented GOES 8 collections. As described in [2], a complex tumbler may return to the same angle ψ at half the full spin period, thus half integer solutions $nT_{\psi}/2$ should also be considered in Equation 11. To determine the most likely complex solution for a GOES 8 collection with suspected values for $\overline{T}$ and $T_{\bar{\phi}}$, a list of candidate T_{ψ} solutions were generated for $n = 1, 2, 3, ..., 20$. Models were generated and ranked by Bayesian evidence for a range of Fourier terms ($n_{f,max}$ = 2, 4, 8, and 10 in Equation 2), with and without a bisection refinement algorithm to optimize the rotation frequencies of candidate solutions.

The results for the Feb 23 collection are in clear agreement for a spin period approximately equal to the quasi-period, with each case through $n_{f,max} = 8$ favoring this solution, and $T_{\bar{\phi}}$ = 218.902 seconds, corresponding to a 5:1 complex spin state resonance. The results provided in [10] corroborate this result using photometric and radar data collected the same week (Feb 18 and 20). Taking the same approach for the May 13 collection proved to be less conclusive. The six $n_{f,max}$ and bisection combinations that were in mutual agreement for the Feb 23 data produced four different preferred spin periods for $T_{\bar{\phi}} = 363.679$ seconds and $\overline{T}$ = 1817.120 seconds. While it's unclear why a consistent solution could not be obtained in this case, a proposed explanation is that the shift in the observing geometry over the course of the significantly longer periods of interest was large enough to make it difficult to fit a fixed, two-frequency model to the light curve.

The Feb 16 GOES 8 collection also shows a quasi-period that is 5 times the suspected precession period of 214.420 seconds. When comparing the resulting candidate models, the preferred spin period is approximately equal to $\overline{T}$ or $\overline{T}/2$ for six of the eight combinations tested. The Feb 21 collection is significantly shorter than other GOES 8 observations, but without being able to identify a quasi-period from folding the light curve it is reasonable to suspect that $\overline{T} = 5T_{\bar{\phi}}$ here as well. Unfortunately, a consistent spin period was not found from fitting candidate models to this data.

The May 15 light curve shows a quasi-period of approximately 1845 seconds, or five times the suspected precession period as well. Testing candidate solutions derived from this period produces inconclusive results; again this may be due to the length of the periods involved and phase angle changes, or perhaps the orientation of the axis of precession during this week of collections. While the inability to obtain a definitive result for the spin period for either of the May 2020 GOES 8 collections limits the confidence in this claim, it seems very likely that GOES 8 continues to maintain the 5:1 tumbling period resonance that was found for the February 2020 collections. This is supported by the quasi-period that was identified for both the May 13 and 15 collections, as well as the dynamical simulation work performed by Benson at el. [10] A summary of the GOES 8 complex spin state modeling is provided in Table 1.

4. SUMMARY

Building upon established physics-based algorithms for characterizing the periodicity and spin state of non-resolved objects in Earth orbit, the theory and algorithms used to generate models of light curves of tumbling deep space objects have been presented. Observations of the retired GOES 8 satellite provide an excellent means of testing this capability. Observations across five nights spanning February through May 2020 were collected, from which the complex spin state of GOES 8 was readily discerned by comparing two-dimensional Fourier series models to the single frequency case describing a stable spinner. By combining information gleaned over multiple nights, and considering known

Approved for public release; distribution is unlimited. Public Affairs release approval #AFRL-2021-3059.

symmetry information about the satellite shape, spin and precession periods were determined for each collection. Over the span of three months, the period of precession increased by more than 2 minutes, from 214.569 seconds on 16 Feb 2020 to 369.045 seconds on 15 May 2020, while the spin period increased from 1054.97 seconds to 1845 seconds over that time frame. Future work might hope to fully understand the conditions required for optimal determination of multi-frequency light curve models for objects in complex rotation states.

5. REFERENCES

[1] C. Benson, D. J. Scheeres, and N. Moskovitz. Light curves of retired geosynchronous satellites. *Proceedings of the 7th European Conference on Space Debris*, 2017.

[2] Conor J. Benson, Daniel J. Scheeres, William H. Ryan, and Eileen V. Ryan. Cyclic complex spin state evolution of defunct GEO satellites. *Proceedings of the Advanced Maui Optical and Space Surveillance Technologies Conference*, 2018.

[3] Conor J. Benson, Daniel Scheeres, William H. Ryan, Eileen V. Ryan, and Nicholas A. Moskovitz. GOES spin state diversity and the implications for GEO debris mitigation. *Acta Astronautica*, 167(167):212–221, 2020.

[4] Doyle Hall, John Africano, David Archambeault, Brian Birge, David Witte, and Paul Kervin. AMOS observations of NASA's IMAGE satellite. *Proceedings of the Advanced Maui Optical and Space Surveillance Technologies Conference*, 2006.

[5] Applied Optimization. *Electro-Optical Space Situational Awareness (EOSSA) File Format Description Document, Version 3.1*, December 2013.

[6] Doyle Hall and Paul Kervin. Optical characterization of deep-space object rotation states. *Proceedings of the Advanced Maui Optical and Space Surveillance Technologies Conference*, 2014.

[7] P. Pravec, A. W. Harris, P. Scheirich, P. Kusnirak, L. Sarounova, C. W. Hergenrother, S. Mottola, M. D. Hicks, G. Masi, Yu.N. Krugly, V.G. Shevchenko, M.C. Nolan, E.S. Howell, M. Kaasalainen, A. Galad, P. Brown, D.R. DeGraff, J.V. Lambert, W.R. Cooney Jr., and S. Foglia. Tumbling asteroids. *Icarus*, 173:108–131, 2005.

[8] Antonella A. Albuja, Daniel J. Scheeres, and Jay W. McMahon. Evolution of angular velocity for defunct satellites as a result of YORP: An initial study. *Advances in Space Research*, 56:237–251, 2015.

[9] Antonella A. Albuja, Daniel J. Scheeres, Rita L. Cognion, William Ryan, and Eileen V. Ryan. The YORP effect on the GOES 8 and GOES 10 satellites: A case study. *Advances in Space Research*, 61:122–144, 2018.

[10] Conor J. Benson, Charles J. Naudet, Daniel J. Scheeres, Joseph S. Jao, Lawrence G. Snedeker, William H. Ryan, Eileen V. Ryan, Marc A. Silva, and Jeffrey K. Lagrange. Radar and optical study of defunct geo satellites. *Proceedings of the Advanced Maui Optical and Space Surveillence Technologies Conference*, 2020.

Approved for public release; distribution is unlimited. Public Affairs release approval #AFRL-2021-3059.